

# Equilibrium properties of spherical torus plasmas in NSTX

S.A. Sabbagh<sup>a</sup>, S.M. Kaye<sup>b</sup>, J. Menard<sup>b</sup>, F. Paoletti<sup>a</sup>, M. Bell<sup>b</sup>, R.E. Bell<sup>b</sup>,  
J.M. Bialek<sup>a</sup>, M. Bitter<sup>b</sup>, E.D. Fredrickson<sup>b</sup>, D.A. Gates<sup>b</sup>, A.H. Glasser<sup>c</sup>,  
H. Kugel<sup>b</sup>, L.L. Lao<sup>d</sup>, B.P. LeBlanc<sup>b</sup>, R. Maingi<sup>e</sup>, R.J. Maqueda<sup>c</sup>, E. Mazzucato<sup>b</sup>,  
D. Mueller<sup>b</sup>, M. Ono<sup>b</sup>, S.F. Paul<sup>b</sup>, M. Peng<sup>e</sup>, C.H. Skinner<sup>b</sup>, D. Stutman<sup>f</sup>,  
G.A. Wurden<sup>c</sup>, W. Zhu<sup>a</sup>, NSTX Research Team

<sup>a</sup> Department of Applied Physics and Applied Mathematics, Columbia University,  
New York, N.Y.

<sup>b</sup> Princeton Plasma Physics Laboratory, Princeton University, Princeton, New Jersey

<sup>c</sup> Los Alamos National Laboratory, Los Alamos, New Mexico

<sup>d</sup> General Atomics, San Diego, California

<sup>e</sup> Oak Ridge National Laboratory, Oak Ridge, Tennessee

<sup>f</sup> Johns Hopkins University, Baltimore, Maryland

United States of America

**Abstract.** Research in NSTX has been conducted to establish spherical torus plasmas to be used for high  $\beta$ , auxiliary heated experiments. This device has a major radius  $R_0 = 0.86$  m and a midplane halfwidth of 0.7 m. It has been operated with toroidal magnetic field  $B_0 \leq 0.3$  T and  $I_p \leq 1.0$  MA. The evolution of the plasma equilibrium is analysed between discharges with an automated version of the EFIT code. Limiter, double null and lower single null diverted configurations have been sustained for several energy confinement times. The plasma stored energy reached 92 kJ ( $\beta_t = 17.8\%$ ) with neutral beam heating. A plasma elongation in the range  $1.6 \leq \kappa \leq 2.0$  and a triangularity in the range  $0.25 \leq \delta \leq 0.45$  have been sustained, with values of  $\kappa = 2.6$  and  $\delta = 0.6$  being reached transiently. The reconstructed magnetic signals are fitted to the corresponding measured values with low errors. Aspects of the plasma boundary, pressure and safety factor profiles are supported by measurements from non-magnetic diagnostics. Plasma densities have reached 0.8 and 1.2 times the Greenwald limit in deuterium and helium plasmas, respectively, with no clear limit encountered. Instabilities including sawteeth and reconnection events, characterized by Mirnov oscillations, and a perturbation of the  $I_p$ ,  $\kappa$  and  $l_i$  evolutions, have been observed. A low  $q$  limit was observed and is imposed by a low toroidal mode number kink instability.

## 1. Introduction

Spherical tori, very low aspect ratio variants of standard tokamaks, offer potential advantages as fusion energy reactors [1]. The most attractive ST reactor designs have both high fusion power and high bootstrap current fraction. To achieve this operation, both high toroidal  $\beta$ ,  $\beta_t \equiv 2\mu_0 \langle p \rangle / B_0^2$ , and high normalized  $\beta$ ,  $\beta_N \equiv 10^8 \langle \beta_t \rangle a B_0 / I_p$ , are required.

Stable experimental high  $\beta_N$  ( $< 6$ ) ST equilibria have been demonstrated in the START [2] device. The promising results obtained in this relatively small scale machine (plasma current  $I_p = 0.3$  MA) have encouraged the recent construction and initial operation of larger ST devices such as MAST [3] and NSTX [4]. These machines are capable of operating with increased plasma current of 1 MA or

greater. Auxiliary heating power systems for NSTX are designed to exceed 10 MW.

In any new device, a primary goal is to establish reproducible plasma configurations required for future experimentation. A basic and essential component of the analysis of these configurations is the accurate reconstruction of free boundary MHD equilibria based on experimental measurements. The techniques used to reconstruct NSTX equilibria are described in Section 2. The experimental production of the main equilibrium configurations envisioned during the design phase of NSTX, along with the response of the equilibrium to observed plasma phenomena, is discussed in Section 3. The observed instabilities and operational limits are also discussed in this section. The ideal MHD stability limits for

NSTX are discussed in Section 4. Conclusions are drawn in Section 5.

## 2. Equilibrium reconstruction technique

Free boundary plasma equilibrium reconstructions were obtained by utilizing the EFIT algorithm, full details of which can be found in Ref. [5]. The technique is summarized below, followed by specific additions and constraints required to model the NSTX configuration.

### 2.1. General technique

The free boundary equilibrium is computed by satisfying MHD force balance through the solution to the Grad–Shafranov equation

$$R^2 \nabla \cdot (\nabla \psi / R^2) = -\mu_0 R J_t \quad (1)$$

in the plasma (inner) region, and matching measured poloidal fluxes, magnetic fields and imposed currents in the force free (outer) region. Here,  $R$  is the cylindrical radial co-ordinate, and  $J_t$  is the toroidal current density in the plasma. The poloidal flux stream function  $\psi$  throughout the entire rectangular computational domain is obtained through a Picard iteration technique in which  $\psi$  is advanced by

$$\begin{aligned} \psi^{(m+1)}(r) = & \sum G(r, r') I_c \\ & + \int_{v(m)} dR' dZ' G(r, r') \mu_0 J_t(R', \psi^{(m)}) \end{aligned} \quad (2)$$

while iteratively minimizing the difference between measured and computed values in a least squares sense

$$\chi^2 = \sum [(M_i - C_i) / \sigma_i]^2 \quad (3)$$

where  $M_i$  is a measured value or other constraint,  $C_i$  is the computed analogue and  $\sigma_i$  is the error associated with the measurement or constraint. Here,  $I_c$  are the imposed currents in external coils and conductors, and  $G(r, r')$  is the toroidal Green function. The Green function is typically computed once for a given modelled system and stored in tabular form for subsequent processing. The toroidal plasma current

$$\mu_0 J_t = \mu_0 R p'(\psi) + ff'(\psi) / R \quad (4)$$

is defined by the two flux functions  $p'$  and  $ff'$ , which are the plasma pressure gradient and poloidal current

functions, respectively, with  $f = RB_t$ . In general, two such flux functions are arbitrary, and an equilibrium solution requires that these two functions be defined. A set of basis functions is used to specify  $p'$  and  $ff'$ , with a set of free parameters used to allow the self-consistent solution of the equilibrium constraint and simultaneous minimization of  $\chi^2$ . As in Ref. [5], a general set of polynomial basis functions is chosen of the form

$$p'(\psi) = \sum A_i \psi_n^i \quad (5)$$

$$ff'(\psi) = \sum B_i \psi_n^i \quad (6)$$

where  $\psi_n$  is the poloidal flux normalized to the poloidal flux between the plasma boundary and the magnetic axis. The specific choice of polynomial order and constraint of these functions for NSTX equilibria is discussed in Section 2.2.

### 2.2. Specific considerations for spherical tori and NSTX implementation

The EFIT code has been applied to many tokamaks, including DIII-D, JET and JT-60U. Each implementation has the specific features required to properly model a particular configuration.

NSTX reconstructions typically utilize data from more than 70 magnetic diagnostics including as many as 9 currents in the shaping and ohmic heating coils, 42 magnetic flux loops, 9 loop voltage monitors, 16 integrated local  $dB/dt$  pick-up coils and a Rogowski coil measuring the total toroidal current in the plasma, vacuum vessel, copper stabilizer plates and lower divertor coil. The poloidal cross-section of the NSTX device, illustrating the diagnostics and conducting structure, is shown in Fig. 1.

Special aspects of the NSTX EFIT implementation are primarily due to the low aspect ratio of spherical tori. In particular, the inclusion of a sufficiently detailed model of the conducting structure in close proximity to the plasma region is generally required in the reconstructions. Since the one turn electrical resistance of vacuum vessel components scales linearly with the major radius, the low aspect ratio NSTX vessel carries a greater induced current for a given applied transformer voltage compared with a conventional aspect ratio tokamak.

The NSTX vacuum vessel and conducting stabilizing plates are modelled as a collection of single turn parallel conductors. The vessel components are divided into 20 independent current carrying regions, and the combination of the passive conducting plates

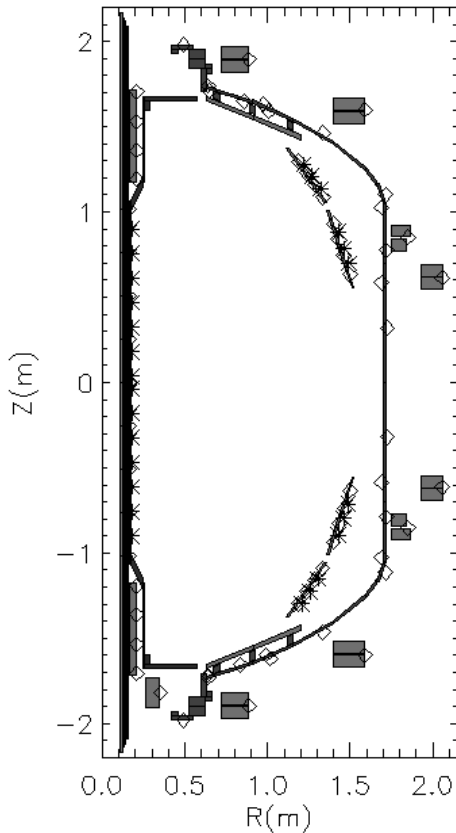


**Figure 1.** Magnetic field coils, conducting structure and magnetic diagnostics of NSTX. Open diamonds represent toroidal flux loops and asterisks represent magnetic field sensors.

and divertor plates is divided into 10 regions. An effective resistance for each region is computed by fitting the vacuum field of NSTX with EFIT. The reconstructed currents in each vessel segment region are then compared with the voltage measured in a neighbouring loop voltage sensor, yielding a resistance,  $R_{eff,i} = V_{loop,i}/I_i$ . The values computed by the fit, and the resulting current distribution in the vessel, agree with equivalent eddy current code calculations. The total computed current agrees with the value measured by the plasma current Rogowski coil within the stated error.

The resistance vector is then used to compute the current for each vessel segment region, given the measured loop voltages, for subsequent reconstructions of the plasma equilibria. These currents are then fitted, along with the other magnetic measurements, when computing the equilibrium solution. Since the discrete loop voltage sensors do not identically reproduce the voltage over the vessel segment region to which they are matched, the computed currents are

input to the reconstruction with relatively large error bars ( $\approx 20\%$ ). This error is small enough to prevent the algorithm from minimizing  $\chi^2$  at an unphysical solution, yet is large enough to permit the solution to deviate from the computed value during periods of fast current transients.

Measurements of the currents in the passive conducting plates and the divertor plates are not yet available. Calculations using the SPARK code [6] of the 3-D eddy currents in these regions during an NSTX discharge indicate axisymmetric equivalent currents that flow in opposing directions in the top and bottom of a given plate. The magnitude of these currents is a few kiloamps. The input to the reconstruction is therefore set at zero current for the plates, with an error of  $\pm 3$  kA to allow currents of this magnitude to flow in these regions. Typically, currents are reconstructed in these regions which may resemble the axisymmetric equivalent current pattern, but the present diagnostic set does not allow reliable reconstruction of these currents. NSTX will be instrumented with additional diagnostics to accurately determine the magnitude of these currents.

Another consideration for the equilibrium fitting is the choice of constraints for the basis function model. The integral relations obtained from the general MHD equilibrium equation generally lead to a solution for  $\Lambda = \beta_p + l_i/2$  [7]. However, for plasmas with a sufficiently non-circular cross-section, Eq. (4) of Ref. [7] can be used to separately determine  $\beta_p$  and  $l_i$  from external magnetic measurements alone. These three equations indicate that three free parameters can be used to describe three global quantities for the equilibrium, typically,  $I_p$ ,  $\beta_p$  and  $l_i$ .

For NSTX plasmas, a reliable basis function set for  $p'$  and  $ff'$  is

$$p'(\psi) = A_1 \psi_n (1 - \psi_n) \quad (7)$$

$$ff'(\psi) = B_0 + B_1 \psi_n - (B_0 + B_1) \psi_n^2. \quad (8)$$

This model, which has three free parameters, constrains the toroidal plasma current at the edge to zero. This is satisfactory to reconstruct quasi-stationary NSTX plasmas; however, it fails to track large fast transients in the current profile, including reconnection events that significantly alter  $l_i$ . Note that this model employs the constraint that  $p' = 0$  at the magnetic axis.

It is found that the finite edge current density can be modelled reliably if one higher order in  $\psi_n$  is allowed in the  $ff'$  profile, and the constraints

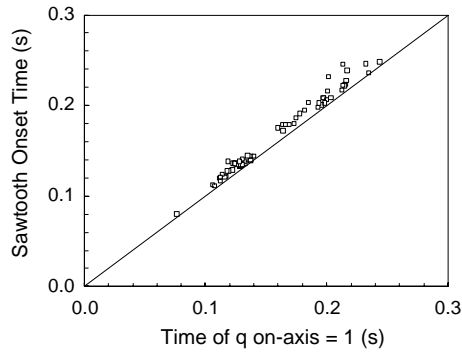


**Figure 2.** Onset time of sawteeth in NSTX versus time of  $q_0 = 1$  crossing from discharge reconstructions.

$p' = 0$  on-axis and  $(ff')' = 0$  at the plasma edge are imposed, the latter constraint allowing for finite edge current density. This model has four free parameters. Normally, allowing this extra degree of freedom requires the imposition of an additional constraint — for example, the safety factor at the magnetic axis  $q_0$ . However, for NSTX, it is found that if the input magnetics have sufficient accuracy and are free of large discrepancies, the extra degree of freedom in  $ff'$  need not have an additional constraint imposed as long as the constraint of  $p' = 0$  on-axis is imposed.

Since measurements of the internal magnetic field are not yet available on NSTX, constraining  $q_0$  is not justified. However, since sawteeth are observed in NSTX plasmas, the time evolution of  $q_0$  can be compared with the appearance of sawteeth. Basis function models of lower order and with different constraints have been tried, and the model given above best correlates the temporal crossing of  $q_0 = 1$  and the onset of sawteeth. This correlation is demonstrated in Fig. 2. For 80 plasmas examined, sawteeth appear when  $q_0 = 0.96 \pm 0.05$ .

The choice of basis function models and vessel current specification described above has sufficient freedom to reconstruct equilibrium quantities such as stored energy with little noise, yet can reproduce fast current perturbations. This prescription is used for between discharge analyses of NSTX plasmas, which typically produce 150 reconstructions per discharge. While the reconstructions cannot always follow some of the larger transients, it is normal for all input magnetics signals to be reproduced within the stated error over the entire evolution of the plasma. A detailed summary of the reconstruction quality is given in the Appendix.

### 3. Experimental results

#### 3.1. Establishing plasma equilibria

Research in NSTX is being conducted to establish the equilibrium configurations to be used in high  $\beta$  experiments with intense neutral beam and high harmonic fast wave heating [8]. The device has a major radius  $R_0$  of 0.86 m and a midplane halfwidth of 0.7 m. The machine has been operated with deuterium or helium gas, with an on-axis vacuum toroidal field  $B_0 \leq 0.3$  T and a plasma current  $I_p \leq 1.1$  MA. Peak electron densities of  $8 \times 10^{19} \text{ m}^{-3}$  have been produced in helium plasmas and  $5.5 \times 10^{19} \text{ m}^{-3}$  in deuterium plasmas. Pulse lengths have been extended to 0.5 s at  $I_p \leq 0.5$  MA. The plasma current and the radial and vertical positions are controlled by real time feedback of the poloidal field coil currents [9] while the plasma shape is presently controlled by pre-programming currents in the poloidal field shaping coils. To minimize impurity influx, the graphite tile surface facing the plasma was conditioned by a glow discharge in a mixture of trimethylboron and helium. Details of the plasma startup and flux consumption before and after the application of boron are given in Ref. [10].

The plasma boundary configurations and the operational space envisioned during the design phase of NSTX have been produced. Limiter, double null and lower single null diverted configurations (Fig. 3) have been created. Each configuration was sustained at a nominally constant  $I_p$  for a duration of several energy confinement times.

These target plasmas have been successfully heated with up to 3 MW of high harmonic fast wave (HHFW) power [8] and separately with 2.8 MW of neutral beam power. In these cases,  $W_{tot}$  has reached 56 kJ ( $\beta_t = 10\%$ ,  $\beta_N = 2.8$ ) and 92 kJ ( $\beta_t = 17.8\%$ ,  $\beta_N = 3.1$ ), respectively, with energy confinement times at peak stored energy (not including shinethrough and other losses) of 15 and 20 ms.

Figure 4 illustrates the evolution of plasma parameters for an ohmic double null diverted plasma with  $I_p = 0.7$  MA. The configuration is maintained for three energy confinement times  $\tau_E$ . The plasma stored energy  $W_{tot}$  reaches 43 kJ, which equates to  $\beta_t = 7.8\%$  at the ohmic input power of 1.1 MW at peak  $W_{tot}$ . The corresponding  $\tau_E$  is 40 ms. Because of the reduced resistance of the low aspect ratio vessel components, the proximity of the conducting structure, and the appreciable loop voltage (2–6 V) used

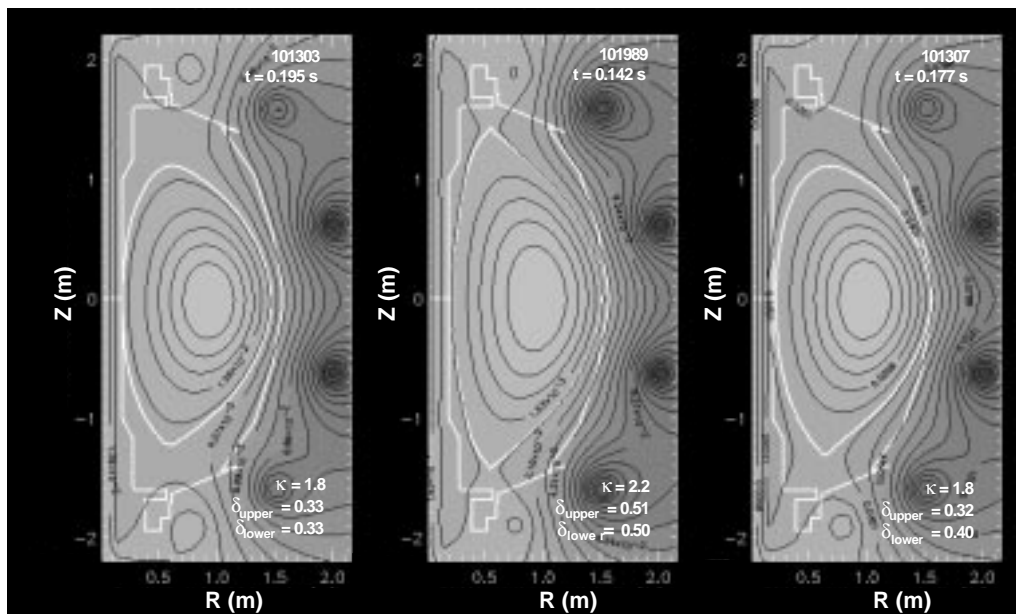


**Figure 3.** Reconstructions of poloidal flux contours for limited, double null and lower single null diverted equilibria.

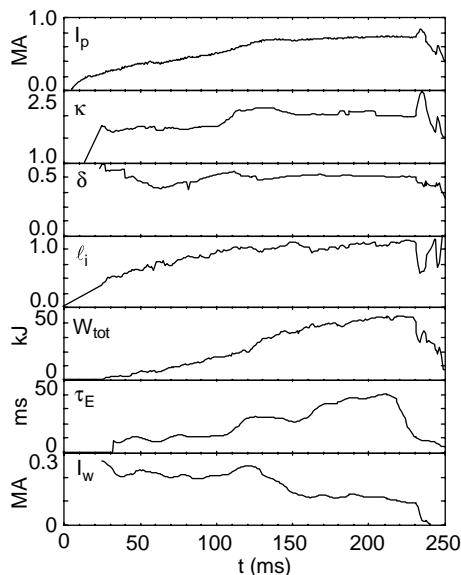


**Figure 4.** Time evolution of EFIT reconstructed plasma parameters for an NSTX ohmic discharge. The interval between reconstructions is 1 ms.

during the  $I_p$  increase, the induced currents flowing in the vacuum vessel wall and stabilizing conducting plates can be significant and are necessarily included in the reconstructions. The induced wall current  $I_w$  varies between 0.2 and 0.25 MA from the first reconstruction at  $t = 25$  ms until peak  $I_p$  is reached. The

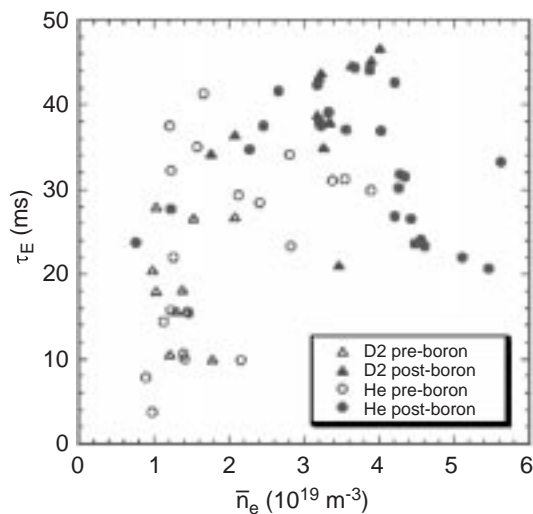


**Figure 5.** Energy confinement time versus line averaged density in deuterium and helium plasmas, pre- and post-boronization.

largest values of  $W_{tot}$  in ohmic plasmas were attained with the highest values of plasma current, electron density  $n_e$  and plasma volume  $V$ . These plasmas are paramagnetic, and, due to the low aspect ratio and low toroidal field of the device, have large magnetic field pitch angles at the plasma edge in excess of  $45^\circ$  at  $I_p = 1$  MA.

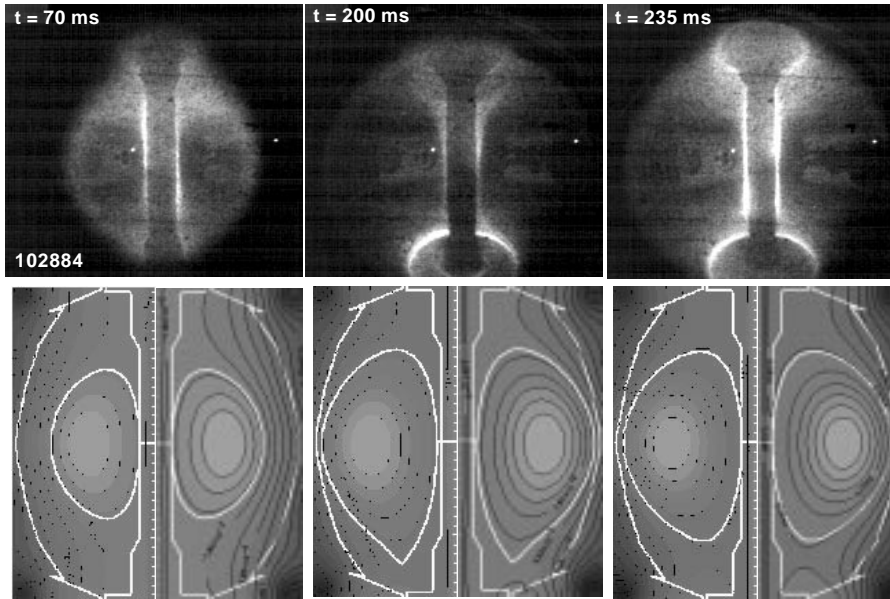


**Figure 6.** Comparison of visible light images of the evolution of the plasma boundary and magnetic reconstructions.

The energy confinement times in both deuterium and helium ohmic plasmas exhibit trends that are similar to those at conventional aspect ratio (Fig. 5). For low to moderate densities ( $\leq 4 \times 10^{19} \text{ m}^{-3}$ , corresponding to  $n_e/n_{e,GW} \leq 0.8$ , where the Greenwald density  $n_{e,GW} \equiv I_p/\pi a^2$ , with  $a$  being the plasma minor radius), the energy confinement time in both species increases approximately linearly with line averaged density to a value of 45 ms. Densities greater than  $4 \times 10^{19} \text{ m}^{-3}$  were attained only in post-boronized helium plasmas, and for these the confinement time is seen to drop to values of about 20 ms at the highest density ( $5.5 \times 10^{19} \text{ m}^{-3}$ , corresponding to  $n_e/n_{e,GW} \approx 1.2$ ). At  $n_e/n_{e,GW} = 0.8$ , the maximum  $\tau_E$  is approximately  $1.4\tau_{E,ITER89P}$ , while  $\tau_E/\tau_{E,ITER89P} = 0.8$ – $1.0$  at the higher densities. For the ITER89P scaling in this case, the mass scaling parameter was taken to be  $M_{eff}/Z_{ion}$ , which is 2 for either species. The confinement time in the post-boronized plasmas was not necessarily greater than that in the pre-boronized plasmas at the same density; boronization, however, served to extend the accessible density range.

### 3.2. Plasma boundary and profiles

As discussed in Section 2.2, the equilibrium reconstructions fit well to the external magnetic measurements. The response of equilibrium parameters to

plasma dynamics and perturbations is reproduced in detail as a function of time, including the general time evolution of  $q_0$ . In addition, aspects of the plasma boundary, pressure and  $q$  profiles that define the plasma equilibria can be assessed using non-magnetic diagnostics.

The evolution of the reconstructed plasma configuration agrees with visible light emission from the plasma imaged at 1 kHz [11]. Figure 6 shows a comparison of these results for events which illustrate the plasma boundary in the fast camera images. An early, small bore plasma evolution, transition to a lower single null diverted plasma and the return of the plasma to the centre stack limiter before shutdown are compared with the boundary reconstructions from magnetics diagnostics. The two bright points in each frame are tungsten filaments. In the first frame, the plasma boundary is in the field of view of the camera. In the remaining frames the boundaries, which are at large major radii, are outside the field of view. In the second frame, the dark centre column, visible scrape-off region and bright lower divertor region indicate a lower single null plasma with a small inner gap. The final frame shows the plasma moving back to the centre column limiter, which becomes bright with a small dark band near the lower portion of the column. These features are all consistent with the details of the reconstructed plasma boundary shape.

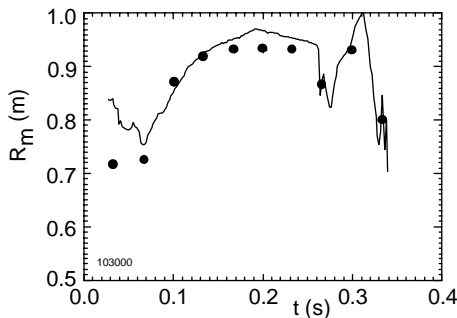


**Figure 7.** Comparison of reconstructed magnetic axis position (curve) and axis position from multipulse Thomson scattering diagnostic (points).

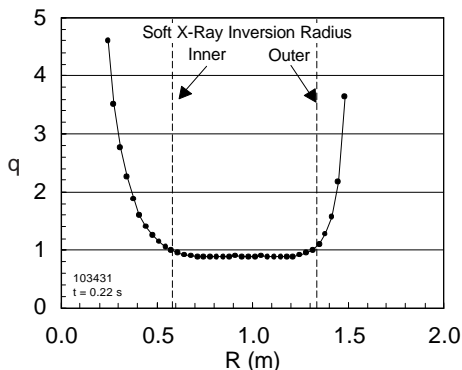


**Figure 8.** EFIT  $q$  profile versus major radius and position of soft X ray inversion radius.

The multipulse Thomson scattering diagnostic yields the time evolution of the electron pressure profile. The energy stored by electrons is typically 40–50% of the total stored energy in ohmic plasmas, as high as 70% in high harmonic fast wave heating (HHFW) plasmas and greater than 25% in plasmas heated with neutral beams. Note that the present Thomson scattering data are based on Rayleigh calibration. Preliminary examination of reflectometer data suggests somewhat lower density.

The magnetic axis position of the electron pressure profile agrees well with the equilibrium analysis. Figure 7 shows the time evolution of the reconstructed magnetic axis and that given by the electron pressure profile. Note that the latter is determined by a spline fit of the pressure using channels that are separated by about 15 cm, so an uncertainty of several centimetres is not unexpected. The two measurements are in agreement through the large reconnection event at  $t = 0.27$  s. The discrepancy at the initial time point shown is due to the electron pressure profile being hollow, and the EFIT

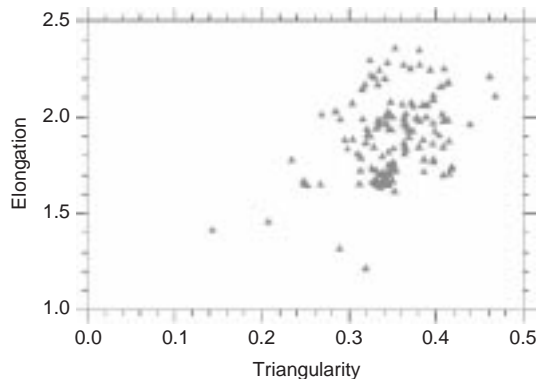


**Figure 9.** Operational space of NSTX boundary parameters at peak stored energy.

reconstruction being less reliable since the plasma current is about equal to the current in the vacuum vessel wall at this early time.

In addition to the  $q_0$  evolution being consistent with the onset of sawteeth (Fig. 2), the position of the inversion radius of the soft X ray signals gives an indication of the radial position of the  $q = 1$  surface. Figure 8 shows good agreement between the radial positions of the EFIT  $q = 1$  surface and the inversion radius from an inversion of 45 soft X ray chords. The plasma has a large  $q = 1$  region, consistent with the observation of a large sawtooth amplitude in this discharge. The operational limits associated with the large sawteeth in this plasma are discussed in the next section.

### 3.3. Operational space and instabilities

A primary objective in establishing the first equilibria in NSTX was to determine the range of boundary shapes possible in the experiment. A plasma elongation of  $1.6 \leq \kappa \leq 2.0$  and a triangularity in the range  $0.25 \leq \delta \leq 0.45$  have been sustained, while maximum values of  $\kappa = 2.6$  and  $\delta = 0.6$  have been reached transiently. A subset of the present NSTX  $(\kappa, \delta)$  database is shown in Fig. 9.

The density limits in NSTX ohmic plasmas were explored in both deuterium and helium by varying the gas puff rates from discharge to discharge. These experiments were conducted in pre- and post-boronized plasmas for both species. Figure 10 shows the achieved line averaged electron density as a function of  $n_{e,GW}$ . As can be seen, the pre-boronized plasmas attain densities of up to only  $0.5n_{e,GW}$  for both deuterium and helium. After the first boronization, the achievable densities were considerably higher, with deuterium plasmas reaching

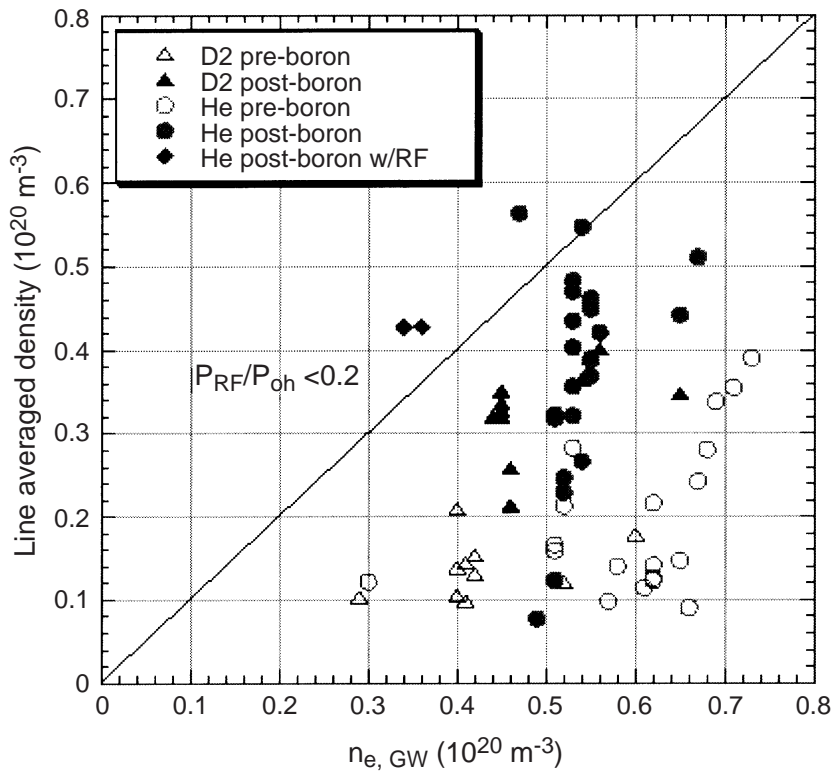


**Figure 10.** Line averaged electron density versus Greenwald density in deuterium and helium plasmas, pre- and post-boronization.

$n_e = 0.8n_{e,GW}$  ( $4 \times 10^{19} \text{ m}^{-3}$ ) and helium plasmas reaching  $1.2n_{e,GW}$  ( $5.5 \times 10^{19} \text{ m}^{-3}$ ). Also shown in the plot are two points from RF heated discharges where  $n_e/n_{e,GW} = 1.2$  but, in these cases, the RF power was less than 20% of the ohmic heating power.

One major difference between deuterium and helium plasmas at higher densities was the amount of carbon III light, which was much greater in deuterium plasmas, presumably due to chemical sputtering of the graphite tiles. For both species, in each of the pre- and post-boronized plasmas, the radiated power was typically  $\leq 30\%$  of the ohmic heating power at the time of maximum density. The only MHD activity observed at the time of the density limit in the highest density cases was sawteeth, and investigations are under way to determine whether the limit is related to the sawteeth, or whether fuelling limitations set the maximum density.

Instabilities characterized as reconnection events, both internal and global, in previous spherical tori experiments [12] have been observed in NSTX during both the increase and the reduction of the plasma current. Evidence of these events is provided by Mirnov oscillations, spikes in the  $I_p$  evolution,  $D_\alpha$

and carbon III light, and, when sufficiently large, alterations of the plasma internal inductance and elongation. For events close to the end of the pulse (leading to, or during the ramping down of  $I_p$ ) a large transient decrease of  $l_i$  (of up to 50%) can occur, with a simultaneous increase in the elongation. Animation of the poloidal flux contours shows that both the boundary and the inner flux surfaces elongate in a similar fashion.

A low  $q$  limit was encountered at  $q_{cyl} = 2.5a^2B_t(1 + \kappa^2)/RI_p \approx 1.4$  by ramping down  $B_t$  at constant plasma current. This limit is manifested by a low toroidal mode number kink instability that terminates the discharge. The low  $n$  non-axisymmetric nature of the mode is apparent from 1 kHz sampled visible light images of the plasma. At the onset of instability,  $\beta_t$  and  $\beta_N$  were 9 and 1.7%, respectively, at  $B_0 = 0.18 \text{ T}$ .

At present, a global  $\beta$  limit has not yet been conclusively reached in NSTX. Fast termination of discharges at relatively high  $\beta$  has been observed in neutral beam heated discharges with a large rate of rise in the plasma stored energy ( $dW_{tot}/dt = 1.3\text{--}2 \text{ MW}$ ). The termination occurs for a wide range,

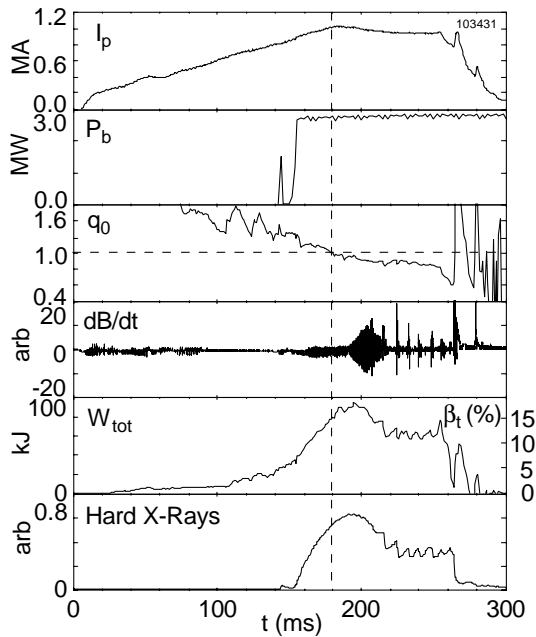


**Figure 11.** Onset of the 1/1 mode and subsequent large sawtooth oscillations in a high  $\beta$  plasma.

$\beta_t \approx 10\text{--}18\%$ , below the values expected for an ideal global kink/ballooning mode. In these plasmas,  $q_0$  drops below unity without a stable sawtooth oscillation. The termination appears to be due to a large reconnection event that would normally be a less perturbative sawtooth oscillation observed in plasmas with less aggressive heating.

The sawtooth oscillation in high  $\beta$  plasmas can also lead to a saturation and rollover of the plasma stored energy. This is illustrated in Fig. 11. Approximately 20 ms after the start of 2.7 MW of NBI heating,  $q_0$  is observed to fall below unity. At this time, a small  $m/n = 1/1$  mode commences and continues to grow. The peak  $W_{tot}$  is reached as the oscillation increases in magnitude, and finally the plasma suffers a large sawtooth crash. The change in  $W_{tot}$  is 15 kJ during the first cycle, which is 20% of the stored energy before the crash. The magnitude of the oscillation is evident in the  $W_{tot}$  waveform until the terminating reconnection event occurs. The detail of the evolution of  $W_{tot}$  is identical to the evolution of the hard X ray detector during this period of time.

#### 4. Ideal stability limits

With equilibrium profiles optimized for ideal MHD stability, NSTX can theoretically achieve  $\beta_t$  in excess of 40% [13]. Studies utilizing profiles from

neutral beam heated tokamak and spherical tori experiments show that while these high  $\beta$  targets are possible, a limit to either high  $n$  ballooning or low  $n$  kink/ballooning modes might be observed at significantly lower values between 20 and 25% [14, 15].

Auxiliary heated NSTX plasmas that have reached  $\beta_N = 2.8\text{--}3.1$  have been used to determine the ideal stability limit by fixing the plasma boundary and scaling the pressure profile self-similarly. The DCON [16] and GATO [17] ideal stability codes were used to compute the low  $n$  stability for these high  $\beta$  equilibria with  $q_0 = 1.2$ . The extrapolated equilibrium is unstable at  $\beta_N = 4.7$  in a double null configuration and at  $\beta_N = 4.5$  in a single null configuration to a global kink/ballooning mode. This mode has a strong internal component, so for these particular equilibria, the stabilizing conducting plates do not significantly alter the  $\beta$  limit.

Future NSTX research will include testing computed stability limits, and determination of the scaling of these limits on the basis of global as well as profile parameters.

#### 5. Conclusions

Spherical torus equilibria have been established experimentally in NSTX, and the time evolutions of these equilibria are now typically reconstructed between discharges using the EFIT algorithm. The techniques used for standard aspect ratio tokamak equilibrium reconstruction have been supplemented for accurate discharge modelling in the spherical torus geometry. A model of the NSTX stabilizing plates, vacuum vessel and other conducting structure is required for accurate reconstructions, as well as the ability of the profile basis functions to allow a finite edge current. The technique has been refined such that measurement errors of the order of one per cent are matched for about 70 measurements, at nearly all reconstruction times, in all configurations and heating schemes, with the same profile basis function model.

Limiter, double null and single null diverted configurations sustained for several energy confinement times have been produced and reconstructed. The plasma current attained has exceeded the conceptual design goal of 1 MA and, within a few weeks of the start of neutral beam operation, has attained high toroidal  $\beta$  values of nearly 18%, at a  $\beta_N$  of 3.1. Densities exceeding the Greenwald limit have been reached, and energy confinement times of 1.4 times the ITER89P scaling have been achieved. Aspects

**Table 1.** Summary of experimental measurement errors and normalized differences between measured and reconstructed signals

Signal group	Mean error		Mean	
	Absolute	Relative (%)	$\xi$	$\xi^2$
OH/shaping coils	38.9 A	0.56	-0.04	0.01
Flux loops (CS)*	6.3 mWb	0.96	0.61	0.54
Flux loops (other)	3.9 mWb	1.22	0.042	0.49
Integrated $dB/dt$ coils	1.0 mWb	2.27	-0.11	0.27
Plasma Rogowski current	15 kA	1.5	0.68	0.99
Vessel current	20 kA	4.0	-0.63	0.95
Plasma current	10 kA	0.5	1.62	3.30

\* CS, centre stack.

of the evolution of the plasma boundary, magnetic axis position, safety factor profile and magnetic axis  $q$  value are supported by non-magnetic diagnostics.

Plasma instabilities including reconnection events, both local and global, have been observed. At low edge safety factor, a global kink mode has been produced at low  $\beta$ . At present, the most virulent instability at high  $\beta$  appears to be an  $n = 1$  instability, similar to a sawtooth in a standard tokamak. Ideal stability studies of the computed equilibria have just begun, and will be refined and automated for future analysis of NSTX plasmas.

## Appendix

### Reconstruction quality

An ensemble of 1500 EFIT reconstructions was run to examine the analysis for large systematic mismatches between experimentally measured and reconstructed signals. These reconstructions comprise the time evolution of seven different NSTX discharges, beginning at  $t = 25$  ms (when the plasma current typically reaches 100 kA, approximately half of the vessel current) until discharge termination. These discharges spanned a large range of plasma parameters and included a plasma heated with HHFW power.

The results are summarized in Table 1. Here, the average absolute and relative errors are given for each measurement group, along with the mean

$$\xi = \frac{1}{N} \sum_i \frac{M_i - C_i}{\varepsilon_i}$$

and the mean

$$\xi^2 = \frac{1}{N} \sum_i \left( \frac{M_i - C_i}{\varepsilon_i} \right)^2.$$

Here,  $\varepsilon_i \equiv [A_j^2 + (R_j M_i)^2]^{1/2}$  is the error associated with each measurement, with  $A_j$  and  $R_j$  being the absolute and relative errors, respectively, for each signal, and  $N$  being the number of reconstructions. In the full analysis, errors were specified for each signal individually. Measurements with values approaching the level of the absolute error are occasionally not useful after the absolute error level is reached. To handle this situation, an additional error specification is used. Measurement values below the stated threshold value are given an absolute error equal to this threshold value. The threshold values are typically 1–3 times the stated absolute error. Approximately 2% of the measurements taken fall below the threshold value for the data set used.

The table shows that while the errors specified for the signals are low, there are no gross systematic or unexpectedly large random uncertainties. The centre stack (CS) flux loops show a very small systematic error which is primarily caused by mismatch of the ohmic heating coil current. The plasma current reconstruction is also a special case in NSTX, since the plasma Rogowski coil measures the sum of the plasma current, the vessel and plate currents, and the lower divertor coil current. The vessel and divertor coil currents are subtracted out in the magnetics calibrations, and the reconstructions are fitted to the resulting value for  $I_p$ . The match to the plasma Rogowski current, adding in the calculated vessel current, falls within  $\xi^2 = 1$ . The small systematic tendency of the measured Rogowski current to be greater than the computed value ( $\xi = 0.68$ ) is

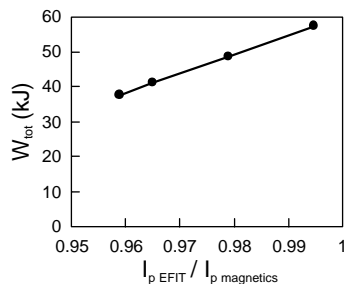


**Figure 12.** Response of  $W_{tot}$  to variations in the ratio of the reconstructed to the measured plasma current.

due to the fitting of the integrated  $dB/dt$  coils, which tend to reduce the computed current. A balance is made between the fitted  $I_p$  in EFIT and the current due to the  $dB/dt$  coils, by artificially reducing the error bar on the input  $I_p$  to the 10 kA/0.5% values indicated. The values indicated produce an average ratio of the EFIT computed  $I_p$  to the difference of the Rogowski and vessel currents of 0.97, taken at the peak in the plasma stored energy, for the seven discharges considered.

A 20% uncertainty in the plasma stored energy is estimated for a plasma similar to that shown in Fig. 4 by examining the effect of systematic discrepancies between the plasma Rogowski and integrated  $dB/dt$  coil measurements. Figure 12 illustrates the variation of  $W_{tot}$  as a function of the ratio between the reconstructed plasma current and the measured value input to EFIT. On the basis of the uncertainty in the measured  $I_p$ , it is expected that this ratio be between 0.97 and 0.98. However, ratios as high as 1 and as low as  $\approx 0.96$  cannot be precluded by the results of the reconstructions. The response of  $W_{tot}$  over this range is shown in Fig. 12 and used to produce an error estimate of  $\pm 10$  kJ. Because of the small error bars on the input magnetic signals, it is expected that random error analysis will yield a much lower uncertainty in the plasma stored energy.

## Acknowledgements

This research was supported by the US Department of Energy under Contract Nos DE-FG02-99ER54524 and DE-AC02-76CH03073.

## References

- [1] Stambaugh, R.D., et al., *Fusion Technol.* **33** (1998) 1.
- [2] Sykes, A., et al., in *Plasma Physics and Controlled Nuclear Fusion Research 1994* (Proc. 15th Int. Conf. Madrid, 1994), Vol. 1, IAEA, Vienna (1995) 719.
- [3] Darke, A.C., et al., *Fusion Technol.* **1** (1995) 799.
- [4] Ono, M., et al., *Phys. Plasmas* **4** (1997) 1953.
- [5] Lao, L.L., et al., *Nucl. Fusion* **25** (1985) 1611.
- [6] Weissenburger, D.W., et al., *SPARK Version 1.1 User Manual*, January 1988, Rep. PPPL-2494, Princeton Plasma Phys. Lab., NJ (1988).
- [7] Lao, L.L., et al., *Nucl. Fusion* **25** (1985) 1421.
- [8] Wilson, H.R., et al., in *Fusion Energy 2000* (Proc. 18th Int. Conf. Sorrento, 2000), IAEA, Vienna (2001) CD-ROM file TH3/5 and <http://www.iaea.org/programmes/ripc/physics/fec2000/html/node1.htm>.
- [9] Gates, D., Mueller, D., Neumeyer, C., Ferron, J., "Control system development plan for the National Spherical Torus Experiment", paper presented at 11th IEEE NPSS Real Time Conf., Santa Fe, 1999.
- [10] Menard, J., et al., in *Fusion Energy 2000* (Proc. 18th Int. Conf. 2000), IAEA, Vienna (2001) CD-ROM file EXP1/05 and <http://www.iaea.org/programmes/ripc/physics/fec2000/html/node1.htm>.
- [11] Maqueda, R., Wurden, G., *Nucl. Fusion* **39** (1999) 629.
- [12] Sykes, A., et al., *Nucl. Fusion* **32** (1992) 694.
- [13] Menard, J., et al., *Nucl. Fusion* **37** (1997) 595.
- [14] Paoletti, F., et al., in *Controlled Fusion and Plasma Physics* (Proc. 25th Eur. Conf. Maastricht, 1999), Vol. 23J, European Physical Society, Geneva (1999) 1709.
- [15] Paoletti, F., et al., *Impact of MHD Equilibrium Input Variations on the High Beta Stability Boundaries of NSTX*, submitted to *Nucl. Fusion*.
- [16] Glasser, A.H., Chance, M.S., *Bull. Am. Phys. Soc.* **42** (1997) 1848.
- [17] Bernard, L.C., Helton, F.J., Moore, R.W., *Comput. Phys. Commun.* **24** (1981) 377.

(Manuscript received 5 October 2000

Final manuscript accepted 24 April 2001)

E-mail address of S.A. Sabbagh:  
sabbagh@pppl.gov

Subject classification: B0, Tm; C0, Tm;  
F1, Te